Nanoscale

Accepted Manuscript

This article can be cited before page numbers have been issued, to do this please use: N. García-Romeral, A. Morales-Garcia, F. Viñes and F. Illas, *Nanoscale*, 2025, DOI: 10.1039/D5NR02231B.

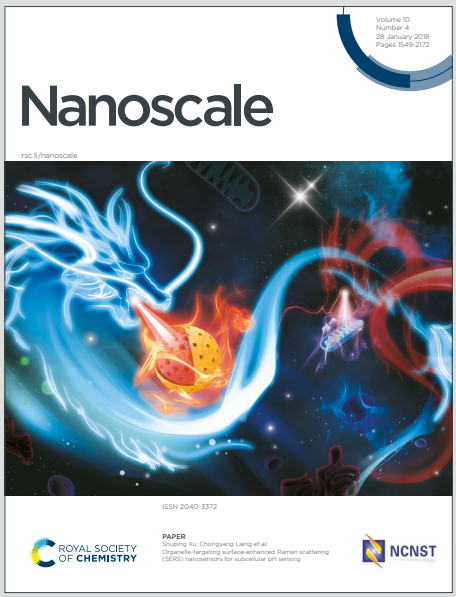

ROYAL SOCIETY OF CHEMISTRY

rsc.li/nanoscale

Cutting Edge(s): Towards Realistic Modelling of MXenes Flakes†

View Article Online
DOI: 10.1039/D5NR02231B

Néstor García-Romeral, Ángel Morales-García,* Francesc Viñes, Francesc Illas

Departament de Ciència de Materials i Química Física & Institut de Química Teòrica i Computacional (IQTCUB), Universitat de Barcelona, c/ Martí i Franquès 1-11, 08028 Barcelona, Spain.

Abstract

We investigate the structural, energetic, electronic, and magnetic properties of newly designed and realistic Ti_2C MXene flakes models using Density Functional Theory (DFT) calculations. By means of Wulff construction procedure, we model flakes that closely resemble experimentally synthesized structures, exhibiting a hexagonal morphology dominated by the thermodynamically stable $(11\bar{2}0)$-nonpolar surface. As the flake size increases, structural parameters and relative stability converge toward periodic Ti_2C slab behaviour, with diminishing quantum confinement effects. Electronic structure calculations reveal a gapless nature across all sizes, with negligible confinement effects on optical properties, even under different magnetic configurations. Hybrid HSE06 calculations predict a slight increase in the band gap compared to PBE, yet this gap vanishes in larger flakes, aligning with periodic slab behaviour, while the band edges energy decreases as the flake size increases. Spin-polarized calculations confirm an antiferromagnetic (AFM) ground state for all flakes, with energy differences between AFM, nonmagnetic (NM), and ferromagnetic (FM) states increasing with increasing size. Notably, for smaller $(Ti_2C)_n$ flakes ($n < 90$), AFM and FM configurations are nearly degenerate, whereas for larger flakes ($n \geq 90$), AFM becomes the definitive ground state. Functionalization of the basal plane with oxygen stabilizes Ti_2CO_2 flakes, inducing structural edge bending, suppressing magnetism, and favouring an NM ground state. The band gaps in functionalized flakes exhibit size-dependent narrowing due to the presence of edge surfaces, diverging from periodic slab trends due to the change of energy of the electronic states. This work provides more realistic, physically meaningful models that offers new insights beyond conventional periodic approaches.

*E-mail: angel.morales@ub.edu

† Electronic supplementary information (ESI) available. See DOI:

View Article Online
DOI: 10.1039/D5NR02231B

1. Introduction

MXenes constitute a class of two-dimensional (2D) transition metal carbides, nitrides, and carbonitrides. This low-dimensional family was discovered back in 2011 by Naguib *et al.*[1] who were able to synthesize Ti_3C_2, the first MXene prototypical example, containing five atomic layers only —excluding terminations, see below. Since then, the number of MXenes has considerably grown and many applications such as in catalysis, biomedicine, and energy storage were envisaged.[2-4] MXenes are generally synthesized through the selective chemical etching of three-dimensional (3D) ternary layered MAX phases with general $M_{n+1}AX_n$ chemical formula, where M represents an early transition metal, A is an element from groups XIII or XIV, X is either carbon (C) and/or nitrogen (N), and *n* (ranging from 1 to 4) determines the thickness of the resulting material.[5-7] After the etching process, the formed MXene chemical formula becomes $M_{n+1}X_nT_x$, where T_x represents surface termination groups (functional groups) attached to the MXene basal plane arising from to synthesis conditions. Termination groups typically include–F, –H, –O, and –OH when using as etching agent hydrofluoric acid or *in-situ* HF.[3,4] Note that additional processing or alternative etching can further remove these groups,[8,9] resulting in pristine MXene surfaces, denoted by $M_{n+1}X_n$.[3,10]

From the point of view of physical and chemical properties, MXenes stand out from other 2D materials due to their wide and vast range of properties. Most of them present a metallic character with no band gap in their electronic structure.[11-14] Nevertheless, as expected, their properties strongly depend on their composition, thickness, and surface terminations.[2] Among the different applications of MXenes, the most relevant ones are as an electromagnetic interference shielding materials,[15-17] their use in lubrication,[18,19] in alkali-ion batteries,[10,20-22] thermo-, electro-, and photo-catalysis,[14,23-27] and gas- and bio-sensors.[28,29]

From the theoretical and modelling point of view, the vast majority of studies regarding MXene properties represent these materials by means of periodic models, with a perfect, infinite surface free of defects, except if they are introduced *ad-hoc* in the unit cell. While this type of model has provided invaluable physical and chemical insights, one must realize that experimentally synthesized MXenes possess finite sizes and exhibit different morphologies where edges are always present. In fact, only a few works deal with the importance of MXenes edge effects. Some authors used models featuring edges through considering large unit cells representing MXene nanoribbons (1D),[30-32] and there is at least one example of using quantum dots (0D)[33] obtained *via* cutting the periodic model as usually made to study graphene structures. These previous works studied the edge effects on some MXene physical properties,

View Article Online
DOI: 10.1039/D5NR02231B

including the importance of edges on the hydrogen evolution reaction by means of MXene nanoribbon models.[34]

Clearly, the possible MXene edge role is still in its infancy, and a more systematic approach is needed to provide more realistic atomistic models from a well-defined procedure. To this end, we propose here a new approach to model pristine MXene flakes more similar to those observed in the experiments. The approach is based on the well-known Wulff construction[35] which takes into account materials crystal structure, symmetry, and superficial energies to define likely shapes minimizing the overall model surface energy. This approach has been successfully used by different authors to model oxide nanoparticles of CeO_2, TiO_2 and ZnO, either anhydrous or hydroxylated,[36-41] and metallic systems.[42-44] From the initial Wulff construction-based flake models, a more realistic atomic structure can be obtained by means of the Density Functional Theory (DFT) optimizations, and subsequently used to study the effect of the quantum confinement and size-dependent properties of interest such as the relative stability, energy formation, and the electronic structure. In the present work, this approach is applied to build and analyse Ti_2C flakes with a broad range of increasing sizes.

2. Building MXenes flakes models and computational details

To investigate the effect of size and morphology on MXene flakes, we take Ti_2C as a case, prototype example. This selection is motivated by *i*) composition, Ti-derived MXenes constitute the workhorse in atomic modelling, and *ii*) due to this 3-layer system behaves similar to its 5-layer (Ti_3C_2) counterpart from a physical and chemical point of view, allows us to reduce the dimensionality optimizing the computational cost. The workflow starts by optimizing the structure of the $c(1\times1)$ conventional unit cell of the ABC-stacked bare Ti_2C featuring two basal planes with (0001) Miller indexes (see Fig. 1a). Next, to obtain the surface energies necessary to model the Wulff construction, the $c(1\times1)$ has been expanded to a $c(3\times3)$ and optimized again. From this supercell, several stoichiometric nanoribbons were created along the only two sets of non-equivalent crystallographic planes, $\{10\bar{1}0\}$ and $\{11\bar{2}0\}$. Due to the inherent ABC stacking of the bare Ti_2C, there are two non-equivalent types of parallel ($11\bar{2}0$) planes. By cleaving the MXene through this plane, two different surfaces can be generated, differing in the atoms they expose. These are a non-polar surface exposing Ti and C atoms and a polar surface exposing C atoms on one side of the cut and only Ti atoms on the other side (see Fig. 1c). In the following, these surfaces are denoted as $(11\bar{2}0)$-nonpolar and $(11\bar{2}0)$-polar, respectively. As a result, three different nanoribbons are possible among which one

corresponds to cutting along the $(10\bar{1}0)$ plane with a width of 5.7 Å (see Fig. 1d), and two to cutting along the $(11\bar{2}0)$, both with a width of 14.5 Å (see Figs. 1e,f). Once the atomic structure of the three nanoribbons is obtained from geometric optimizations as indicated in the next section, the required surface energy (γ) values relative to the periodic MXene model are calculated as

$$\gamma = (E_{nanorib} - n * E_{Ti_2C-slab})/2S \quad (1),$$

where $E_{nanorib}$ is the total energy of the modelled nanoribbon; $E_{Ti_2C-slab}$ is the energy of the Ti_2C $c(1\times1)$ cell; n stands for the number of Ti_2C units of the nanoribbon relative to the Ti_2C $c(1\times1)$ unit cell, and S is the surface area created by the cutting of the $(10\bar{1}0)$ and $(11\bar{2}0)$ surfaces. Note in passing by that in order to calculate the $(11\bar{2}0)$-polar surface energy, a dipole correction has been considered in the calculations.

To build binary nanoparticles with defined stoichiometry, one can make use the freely available computer code developed by González *et al*.[45] or rely on the *WulffPack* python library,[46] the latter being chosen here. Both make use of symmetry and surface energies which are the necessary ingredients when applying the Wulff construction theorem.[35] A home-made program, using the *WulffPack* python library, has been developed to generate a series of bare Ti_2C flakes with different sizes, ranging from 18 to 168 units of Ti_2C. At this point, one must realize that the flakes constructed may not exhibit the proper $(Ti_2C)_n$ stoichiometry. To this end, a number of isomers have been built removing a C atom from each initial MXene flake model. Due to symmetry reasons, different C atom can be removed from each flake, and thus, the most stable one should be selected. The different isomers considered for each $(Ti_2C)_n$ flake, and their relative stabilities, are shown in Fig. S1 and Table S1, respectively, of the Electronic Supplementary Information (ESI) file. Notably, for all $(Ti_2C)_n$, flakes, the most stable isomer corresponds to the one from whose C atom is removed from flake vertex position. Consequently, this isomer is chosen to carry out all present studies of the size-dependent properties for all flakes.

Once the bare Ti_2C flakes have been modelled, the effect of the surface functionalization with O atoms is further explored. Note in passing that MXenes synthesized via HF etching can typically feature mixed terminations, including –OH and –F, however, we choose the most common –O termination as a case of study. To this end, we selected $(Ti_2C)_{18}$, $(Ti_2C)_{60}$, and $(Ti_2C)_{126}$ as representative cases. For these three flakes, adsorbed O atoms were placed at each hollow metal site of (0001) surfaces, as this is the most favourable adsorption site, always

View Article Online
DOI: 10.1039/D5NR02231B

assuring the global stoichiometry, leading to a CABCA stacking.[13,47] We note that full oxygen termination represents an idealized model, while partial or mixed terminations are more realistic under experimental conditions. Our aim here was to isolate the intrinsic effects of pure oxygen functionalization. Next, the structure of the resulting $(Ti_2CO_2)_{18}$, $(Ti_2CO_2)_{60}$, and $(Ti_2CO_2)_{126}$ flakes has been optimized, with the final structures displayed in Fig. 3. To study possible size-dependent properties of the $(Ti_2CO_2)_n$ flakes, the periodic Ti_2CO_2 slab model (see Fig. 1b), with the same CABCA stacking, has also been considered as a reference of infinite size. It is worth pointing out that the present study focuses on the convergence of flake properties to the periodic slab model limit. Therefore, edge functionalization has not been considered. Note also that, as the flake total surface area is dominated by the basal plane, especially for the large flakes, the effect of the edge functionalization is likely to represent a small perturbation of the reported trends. Nevertheless, one must also point out that edge functionalization can affect the overall stability of the flakes, as previous experimental findings reveal that flakes can take a maximum of oxygen before they decompose.[48] The study of edge functionalization represents an open front worth of future studies specifically addressing the coverage limit.

The atomic and electronic structure of Ti_2C and Ti_2CO_2 periodic slabs, as well as of the $(Ti_2C)_n$ and $(Ti_2CO_2)_n$ flakes, plus their relative stability, have been assessed by means of all electron, DFT based calculations, carried out with the Fritz-Haber Institute *Ab Initio* Materials Simulation (FHI-AIMS) package.[49] The Perdew-Burke-Ernzerhof (PBE) form[50] of the Generalized Gradient Approximation (GGA) density functional was chosen and scalar relativistic effects included through the Zeroth Order Regular Approximation (ZORA).[51,52] This code numerically solves the Kohn-Sham equations by expanding the electron density in a basis set of Numerical Atomic-centred Orbitals (NAOs). From the different sets of NAOs provided by FHI-AIMS, we selected the tier-1/light-grid[53] one which has a quality similar to that of a triple-ζ plus polarization Gaussian Type Orbitals (GTO) basis set.[54] The lattice vectors forces were optimized with analytical stress tensor.[55]

In all calculations, a 10^{-5} eV threshold of self-consistent charge density convergence criterion is used, and all structural optimizations were reached when atomic forces were below 10^{-3} eV/Å, using a sigma value of 0.01 eV of Gaussian broadening for partial occupancies to speed up convergence. Only for periodic slab calculations, a 7×7×1 **k**-point mesh[56] was used, dense enough to sample representatively the Brillouin zone, along with a vacuum space of 30 Å in the normal direction to the MXene (0001) surface —*z* direction—, large enough to avoid

View Article Online
DOI: 10.1039/D5NR02231B

interaction between slab replicas. These periodic calculations were performed to assess convergence trends.

In spite of the fact that previous studies have predicted that the bare Ti_2C material exhibits a magnetic ground state with two ferromagnetic layers coupled antiferromagnetically,[57] all geometry optimizations have been performed without accounting for spin-polarization as this has been shown to have a negligible effect on the structural parameters in MXenes.[12,57] However, for a more accurate description of the properties of the investigated flakes, the relative stability and formation energies are studied with and without spin-polarization. Note also that when the periodic $Ti_2C(0001)$ surface is functionalized, the inherent magnetism of Ti_2C is removed.[12,57,58]

To investigate the effect of the Quantum Confinement (QC) in the properties of these systems, we focus on the averaged coordination number for each species in each MXene flake, the relative stability with respect the periodic slab, the formation energy, the overall energy gap —estimated as the difference between the Kohn−Sham orbital energy of Highest Occupied Molecular Orbital (HOMO) and Lowest Unoccupied Molecular Orbital (LUMO)—, the band edges energy, and the possible magnetism of their electronic ground state. The averaged coordination number for each species in each MXene flake has been determined by means of a home-made program that employs the well-known Atomic Simulation Environment (ASE)[59] python library. The relative stability with respect the periodic slab (ΔE) per formula unit is computed following Eq. 2.

$$\Delta E = \left(E_{flake} - n * E_{Ti_2C-slab}\right)/n \quad (2),$$

where E_{flake} is the total energy of each $(Ti_2C)_n$ flake. On the other hand, the formation energy per formula unit, E_f, is calculated with respect to the most stable bulk phase of each component, as

$$E_f = \left(E_{flake} - \frac{n}{m} E_{graphite} - \frac{2n}{l} E_{Ti-hcp}\right)/n \quad (3),$$

where $E_{graphite}$and E_{Ti-hcp} are the total energies of the unit cells of graphite and Ti metal with a hexagonal close-packed (*hcp*) crystal structure, respectively, and *m* and *l* correspond to the number of atoms in each unit cell of graphite and Ti-*hcp*, respectively.

To estimate the optimal band gap, we use the difference between the HOMO and LUMO states. The limitations of GGA functionals in predicting accurate band gaps arise from their tendency to excessively delocalize electrons.[60,61] Therefore, single-point calculations at the

View Article Online
DOI: 10.1039/D5NR02231B

PBE-level relaxed structures were carried out with the hybrid Heyd–Scuseria–Ernzerhof (HSE06) functional,[62,63] with a 25% of non-local Fock exchange, and a 0.2 Å^{-1} range-separation parameter to account for the short-range interaction term. Previous studies have shown that this hybrid functional is more reliable describing the electronic structure of these systems than PBE.[12,14,57,64]

Finally, to study the effect of the QC in the inherent magnetism, the relative stabilities of each non-spin polarized and spin polarized solutions are assessed. In particular, we focus on energy differences between the non-spin polarized, with a closed-shell configuration (NM or non-magnetic), the antiferromagnetic (AFM), and the ferromagnetic (FM) solutions. Note that previous studies have shown that the ground state of the Ti_2C MXenes is magnetic with one unpaired electron per magnetic centre mainly localized at surface Ti atoms and with an antiferromagnetic coupling of the two ferromagnetic layers of Ti atoms; for more details, see Refs. 12, 57, and 64.

3. Results and Discussion

3.1. Bare $(Ti_2C)_n$ flakes with $18 \leq n \leq 168$.

From the calculated relative surface energies, γ, of 4.93, 4.63, and 5.79 J/m^2 for the $(10\bar{1}0)$, $(11\bar{2}0)$-nonpolar, and $(11\bar{2}0)$-polar surfaces, respectively, and employing the Wulff construction, a series of $(Ti_2C)_n$ flakes with $18 \leq n \leq 168$ flakes have been constructed. Note that, apart from the most stable (0001) surface corresponding to the MXene basal plane, the $(11\bar{2}0)$-nonpolar surface emerges as the most thermodynamically stable one with respect the periodic Ti_2C model, followed by the $(10\bar{1}0)$ and $(11\bar{2}0)$-polar surfaces. Then, from a morphological point of view, the resulting structure acquires a hexagonal shape as shown, for instance, in the optimized $(Ti_2C)_{60}$ flake with the exposed surfaces appropriately labelled in Fig. 2. From it, and according to the Wulff theorem, it is clear that the most stable $(11\bar{2}0)$-nonpolar surface promotes the largest surface exposure perpendicular to the basal plane, providing a global hexagonal shape to the flake, whereas the expression of the $(10\bar{1}0)$ surface is less prominent, just trimming the hexagon vertices.

Fig. 3 gathers all optimized $(Ti_2C)_n$ flakes, including side and top views and their size in nm. After optimization, all $(Ti_2C)_n$ flakes remain flat and preserve the ABC stacking as in the periodic slab models without atoms changing plane and with an average Ti–C distance of ~2.1 Å regardless of the flake size. Interestingly, this value matches the one obtained when using a periodic slab model.[57,65-67] Here, the size of each $(Ti_2C)_n$ flake has been estimated using the

planar diameter, ∅, estimated as the distance of opposing $(10\bar{1}0)$ surfaces. The diameters shown in Fig. 3 indicate $(Ti_2C)_n$ flake sizes ranging from 1.01 to 3.65 nm.

On the other hand, the $(Ti_2C)_n$ flakes size influences directly the average atom coordination as shown in Fig. 4, which necessarily will have an impact on their chemistry as evident from experimental evidence that capping the MXene edge flakes with polyanionic salts reduces the oxidation rate of the synthesized flakes in aqueous solution.[68] It is worth highlighting that in the periodic Ti_2C slab, due to the *hcp* arrangement of Ti atoms, each Ti atom has six Ti in-plane neighbours and three Ti out-of-plane neighbours, with C atoms occupying the octahedral holes in the *hcp* lattice, hence the coordination number of Ti and C atoms in the periodic slab is 12 and 6, respectively. For a better visual understanding of the atomic coordination, a simplified scheme is shown in Fig. S2 in ESI. The larger the size, the closer is the average coordination of Ti and C atoms slowly converging to the periodic slab values.

Regarding the relative stability of the $(Ti_2C)_n$ flakes with respect to the periodic slab model, Fig. 5 (left panel) reports the trend as a function of the flake size. This Fig. 5 shows a characteristic asymptotic trend, decreasing the total energy per formula unit towards the total energy of the periodic slab as the Ti_2C size flake increases. To better understand the energetic stability of a $(Ti_2C)_n$ flakes, ΔE, relative to that of the periodic slab, $E_{Ti_2C-slab}$, we rely on the Spherical Cluster Approximation (SCA),[69] where in principle one can approximate the relative stability of a cluster with respect to the bulk as

$$\Delta E = E_{bulk} + \sum_{i=1} a_i \cdot (n^{-\alpha})^i \quad (4).$$

In the SCA framework, where one is interested on the convergence of ΔE of finite clusters or nanoparticles to the 3D bulk limit, one has $\alpha = 1/3$, reflecting the area to volume ratio,[70] a_i being the fitting parameters, with the first term ($i = 1$) dominating the fit and the rest of terms ($i > 1$) accounting for the particularities of each system, such as surface stress and edge energies contributions.[71-73] In the present case, the periodic limit is a 2D systems and, thus, $\alpha = ½$ and here E_{bulk} corresponds to the energy of the periodic slab, $E_{Ti_2C-slab}$. Further details and the fitting parameters of the trends from the plot in the left panel of Fig. 5 are provided in Table S2 from SI.

Note that, to avoid any bias arising from the choice of a particular solution in the DFT calculations, the relative stabilities are calculated for the NM and AFM flakes with respect the NM and AFM periodic slab, respectively, and both results are included in Fig. 5. This figure clearly shows that including or not spin polarization, leads to the same trend. Nevertheless,

View Article Online
DOI: 10.1039/D5NR02231B

except for the smallest $(Ti_2C)_{18}$ flake, the relative stability of AFM flakes is systematically closer relative to that corresponding to the AFM ground state solution for the periodic than the one for the NM solution. It is worth highlighting that for the $(Ti_2C)_{18}$ flake, due to the QC effect, the relative stability with respect the periodic slab when the AFM solution is taken into account lies above the NM one by 0.1 eV per formula unit. Note also that for $n > 18$, this energy difference per formula unit increases as flake size increases.

Similar trends are found for the formation energy of the most stable isomer per chemical unit as shown in Fig. 5 (right panel). The formation energy decreases towards the periodic slab value with an asymptotic behaviour. Note that the fitting curves are also based on the SCA. This formation energy has also been calculated for NM and AFM solutions, the AFM E_f being systematically more stable than the NM one for all-size $(Ti_2C)_n$ flakes. Here, the QC effect for the $(Ti_2C)_{18}$ flake is not large enough to position the NM E_f below the AFM one. In addition, the difference of formation energies between the AFM and NM solutions becomes larger as the flake size increases. Again, the general trend of the formation energies remains qualitatively the same regardless of the magnetic solution. We find that the formation energy of the periodic Ti_2C value is -0.16 eV (AFM) and -0.01 eV (NM) per Ti_2C unit. The formation energies of the flakes converge toward these values as the size increases, deviating by approximately 0.2–0.3 eV for the largest systems studied, indicating progressive stabilization with increasing size. The fitting parameters corresponding to the formation energies in the right panel of Fig. 5 are reported in Table S2 in the SI.

Next, we analyse the effect of flake size on the electronic structure. The energy gap is calculated from the HOMO-LUMO difference as computed with the PBE and HSE06 functionals. Both AFM and NM solutions have been considered in the calculations with the PBE functional and in both cases the electronic gap is zero except for the $(Ti_2C)_{18}$ flake for which the that the QC effect opens a nearly negligible gap of 0.1 eV in the AFM solution. This finding is in agreement with the gap of the AFM solution for periodic slab also leading a null value.[12] This is also the case for the NM solution where PBE results are also in line with the estimated zero energy gap of the NM periodic slab. Overall, all calculations indicate that the QC effect do not have a noticeable effect on the electronic structure of Ti_2C flakes. To further confirm this conclusion, calculations have been carried out using the hybrid HSE06 functional and considering the NM solution. In all cases, the energy gap becomes of at most 0.1 eV. However, as the flake size increases, the QC effects decrease and, as a consequence, the energy gap becomes zero thus matching the value obtained for the periodic slab with the HSE06

View Article Online
DOI: 10.1039/D5NR02231B

functional which is zero for both NM and AFM solutions.[12] For a more visual depiction, the representation of the charge density of the HOMO and LUMO levels in Fig. S3 from ESI. These results show a delocalized character of the charge density, delocalized on the centre and edges of the flake.

Additionally, further insights into the electronic structure can be obtained by analysing the energy of the band edges. Fig. 6 presents the estimated band edge positions for all flakes, calculated using Kohn-Sham values. These values were determined for both PBE and HSE06 functionals. For the former, antiferromagnetic (AFM) and non-magnetic (NM) solutions have been taken into account whereas for the latter only NM solutions were considered for HSE06. Although QC does not affect the energy gap, it significantly influences the positions of the Kohn-Sham energy levels. Specifically, these levels become increasingly negative as the size of the $(Ti_2C)_n$ system grows, approaching the slab limit which, for the Valence Band Maximum (VBM), are -3.7 eV (AFM at PBE), -4.0 eV (NM at PBE), and -4.3 eV (NM at HSE06), and for the Conduction Band Minimum (CBM) become -3.5 eV (AFM at PBE), -4.0 eV (NM at PBE), and -4.0 eV (NM at HSE06). Note that for the PBE-AFM band edges (middle panel from Fig. 6), a small deviation of the data is observed due to the excessive electronic delocalization typical of the GGA functionals when dealing with some *d* electron localization in the AFM solution as previously reported.[12,57,64] A more detailed picture of the described electronic structure can be obtained from the Density of States (DOS) plots gathered in Fig. S4 from ESI. While the DOS in 0D systems consists of discrete energy levels rather than a continuous distribution, we present these plots to monitor the emergence, broadening, and shifting of edge-related states as the flake size increases. This approach allows us to qualitatively assess trends in electronic structure evolution and compare them to periodic behavior. Analysis of these plots shows that all the bare $(Ti_2C)_n$ exhibit a general gapless metallic electronic structure regardless of the functional used (PBE or HSE6). On the other hand, $(Ti_2CO_2)_n$ flakes display a small energy gap, again regardless of the functional used.

For each flake, we inspect the energy difference between the three magnetic configurations as done for the bare periodic Ti_2C MXene in previous studies.[12,57,64] Table 1 summarizes the normalized PBE energy differences ($\Delta E_{\mathrm{AFM-NM}}$ and $\Delta E_{\mathrm{AFM-FM}}$) per number of Ti_2C units for each Ti_2C flake. The results reveal that for all modelled flakes, $\Delta E_{\mathrm{AFM-NM}}$ consistently adopt negative values, indicating that the AFM solution lies below the NM one. This clearly shows that the magnetic ground state of the periodic Ti_2C slab is preserved even after edges cutting leading to finite flakes. Despite these Ti_2C flakes possess a magnetic ground state, the influence of the QC on the magnetic properties is noticeable promoting a size-

View Article Online
DOI: 10.1039/D5NR02231B

dependent behaviour on the $\Delta E_{\mathrm{AFM-NM}}$, monotonically increasing the relative stability of the AFM solution relative to the NM one as flake size increases and nicely converging towards the periodic slab value of -143 meV/n.[12,57,64] Further analysis of the $\Delta E_{\mathrm{AFM-FM}}$ values in Table 1 also shows a size-dependent behaviour due to the QC. For flakes with n < 90 Ti_2C units, the $\Delta E_{\mathrm{AFM-FM}}$ values are less than |10| meV/n, indicating a negligible energy difference. This suggests that, at these sizes, AFM and FM configurations are energetically competitive. On the other hand, for flakes with $n \geq 90$ Ti_2C units, the $\Delta E_{\mathrm{AFM-FM}}$ values are negative and indicate that the AFM solution lies below the FM one, being energetically favoured, and flakes beyond this size adopt an AFM electronic ground state. Again, these $\Delta E_{\mathrm{AFM-FM}}$ values converge towards the value -28 meV/n corresponding to the periodic slab model.[12,57,64] These findings shed light on the size-dependent magnetic properties of Ti_2C flakes and provide insights into the retention of AFM behaviour in reduced-dimensional MXene systems.

Finally, electrostatic potential isosurfaces were computed employing the HSE06 functional to assess spatial variations in reactivity of flakes with size. As shown in Fig. S5 in the ESI, highly negative potential regions are found at the edges, consistent with enhanced chemical reactivity of the edges.

3.2. Effect of O-termination on the basal plane

Hereby, we explore effect of the basal plane functionalization by O atoms on the properties of the Ti_2C flakes. To this end, $(Ti_2CO_2)_{18}$, $(Ti_2CO_2)_{60}$, and $(Ti_2CO_2)_{126}$ have been selected as representative examples. The O atoms have been placed on both sides of the flake basal planes and initially at hollow-metal sites. After geometry optimization, the CABCA stacking remains unchanged. However, the side view in Fig. 3 shows a clear bending deformation of the plane Ti_2C flake due to the functionalization effect. The calculated deformation energy with respect to the planar geometry of Ti_2CO_2 flake per formula unit is the same for the three considered flakes and around -0.3 eV/n. The bending observed in O-functionalized Ti_2C flakes (Ti_2CO_2) could be attributed to surface stress introduced by the terminal oxygen atoms. These groups distort the local bonding geometry, especially at the edges, and generate an internal strain that favors non-planar geometries. Additionally, the electronegativity imbalance between Ti and O atoms could induce a small surface dipole, which can further destabilize the flat configuration and promote the bending as the flake minimizes its electrostatic energy. This effect is absent in pristine Ti_2C flakes, which maintain planar structures due to their higher structural symmetry and lack of dipolar interactions. Consequently, the bending deformation stabilizes the $(Ti_2CO_2)_n$ flake regardless its size. The average interatomic distances resulting from geometry

View Article Online
DOI: 10.1039/D5NR02231B

optimization is of 2.1, 2.1, and 2.2 Å for $(Ti_2CO_2)_{18}$, $(Ti_2CO_2)_{60}$, and $(Ti_2CO_2)_{126}$, respectively. These values are similar to the one corresponding the Ti_2CO_2 periodic slab which is of 2.2 Å. Similarly, the Ti–O averaged distance for the three slabs is 1.9, 2.0, and 2.0 Å for $(Ti_2CO_2)_{18}$, $(Ti_2CO_2)_{60}$, and $(Ti_2CO_2)_{126}$, respectively, again, similar to the periodic slab value of 2.0 Å. It is worth noting that even though this structural bending is not captured by the averaged interatomic distances, it extends upward towards the surface where the O-termination is exposed, and by symmetry and inherent stacking, downward towards the surface where the O-termination is exposed on the opposite surface. In fact, the highest (lowest) vertical position of a O atom is 0.4, 0.7, and 1.0 Å (-0.3, -1.2, and -1.2 Å) above (below) the O-plane for $(Ti_2CO_2)_{18}$, $(Ti_2CO_2)_{60}$, and $(Ti_2CO_2)_{126}$, respectively.

The effect of O functionalization on the electronic structure is noticeable even if the PBE ground state is NM as in the periodic slab. In fact, the PBE calculated energy gap values for the NM solution are of 0.1, 0.1, and 0.0 eV for $(Ti_2CO_2)_{18}$, $(Ti_2CO_2)_{60}$, and $(Ti_2CO_2)_{126}$, respectively, which are significantly different from the 0.4 eV value corresponding to periodic slab model, as estimated in previous works.[13] Since the PBE functional is known to significantly underestimate the band gap of insulator, the NM solution has been also computed using the HSE06 functional. The HSE06 values show the same trend with decreasing values of 0.7, 0.2, and 0.1 eV for $(Ti_2CO_2)_{18}$, $(Ti_2CO_2)_{60}$, and $(Ti_2CO_2)_{126}$, respectively. This implies that, as the Ti_2CO_2 flake size grows, the energy gap closes itself which unexpected as the QC effect decreases with increasing the size. The reason behind this behaviour is not simple since the optical band gap for the periodic slab predicted by the HSE06 functional is 1.0 eV. Therefore, other effects beyond QC must be playing a role. In fact, the divergence between electronic gap of the finite-size flakes and the reference periodic slab models have been documented in previous studies by Hong *et al*.[31] and Zhou *et al*.[32] using MXene nanoribbon models. These authors unveil the influence of the edge effects on the electronic structure of Ti_2CO_2 nanoribbons, with the appearance of electronic states in the middle of the band gap. These energetically downshift the conduction band minimum, narrowing the band gap as the nanoribbon width decreases. Notably, we represented the charge density of the HOMO and LUMO eigenstates (see Fig. S3 in the ESI). These states appear to be delocalized over the centre of the flake and not localized in the edges, implying that the edge surface formation only influences the energy position of the HOMO and LUMO orbitals and not the nature of these orbitals, narrowing the gap as the flake increases. In addition, a comparison between the pristine Ti_2C and Ti_2CO_2 flakes shows that the HOMO and LUMO levels from Ti_2CO_2 flake seem to be more localized than Ti_2C ones.

View Article Online
DOI: 10.1039/D5NR02231B

Finally, regarding the magnetic properties of the considered Ti_2CO_2 flakes, Table 1 also gathers the ΔE_{AFM-NM} and ΔE_{AFM-FM} values for these flakes as obtained from calculations with the PBE functional. All these calculated values are zero, inferring that each Ti_2C flake losses its magnetic ground state when O atoms functionalize both (0001) surfaces, acquiring a NM ground state, which fully agrees with the results obtained for the periodic Ti_2CO_2 slab model, either using PBE or HSE06 functionals.[57,58]

4. Conclusions

We have investigated the properties of realistically shaped Ti_2C MXene flakes, constructed *via* Wulff construction to reflect experimental morphologies, using DFT-based calculations. Structural, energetic, electronic, and magnetic features were analyzed for flakes of increasing size, including oxygen-functionalized variants. The flakes adopt a hexagonal shape dominated by thermodynamically stable $(11\bar{2}0)$-nonpolar surface with a few $(10\bar{1}0)$ surfaces trimming the hexagon vertices. Indeed, all flakes approach the structural characteristics of the periodic slab, with consistent Ti–C distances of ~2.1 Å across all sizes. The relative stability of the bare flakes approaches that of the infinite slab with increasing size, and the AFM configuration remains the ground state, especially for flakes with $n \geq 90$, where it becomes more energetically favored over NM and FM solutions. Quantum confinement (QC) has a marked influence on smaller flakes, affecting their stability and magnetic properties, but in larger systems its impact diminishes.

Electronic structure calculations show that all Ti_2C flakes remain gapless within the PBE approach, with minimal size-dependent QC effects. On the other hand, calculations with the hybrid HSE06 functional yield small band gaps that vanish with size, reproducing the metallic character of the periodic model. Notably, band edge positions shift with size, suggesting tunability for optoelectronic applications. In addition, the electrostatic potential isosurface predicts that the edges formation promotes enhanced reactivity along the edges. Upon O-functionalization, flakes become non-magnetic and slightly bent, with narrowing size-dependent band gaps that deviate from slab behavior due to edge-induced state shifts.

Overall, the study highlights the relevance of flake size and edge effects on the stability and electronic behavior of MXene materials. We hope that the realistic, physically meaningful, models presented in this work will contribute to better understand the properties of the experimentally synthesized MXene flakes as well as to unveil new aspects of the chemistry of

View Article Online
DOI: 10.1039/D5NR02231B

these materials not easily reachable by periodic models, either of extended surfaces or nanoribbons.

Conflicts of interest

There are no conflicts to declare.

Acknowledgements

This study has been supported by the *Spanish Ministerio de Ciencia e Innovación* and *Agencia Estatal de Investigación* (AEI) MCIN/AEI/10.13039/501100011033 through projects PID2021-126076NB-I00, TED2021-129506B-C22, CNS2024-154493, l*a Unidad de Excelencia María de Maeztu* CEX2021-001202-M granted to the IQTCUB and, in part, from COST Action CA18234, and *Generalitat de Catalunya* 2021SGR00079. Part of the calculations have been carried out on the supercomputers of the *Consorci de Serveis Universitaris de Catalunya* (CSUC). N.G.-R. thanks to the *Generalitat de Catalunya* for a predoctoral contract 2022 FISDU 00106. F.V. is thankful for the ICREA Academia Award 2023 Ref. Ac2216561.

Table 1. Energy difference between the AFM and either NM or FM solutions ($\Delta E_{\mathrm{AFM-NM}}$ and $\Delta E_{\mathrm{AFM-FM}}$, respectively) per formula unit, n, for the scrutinized $(Ti_2C)_n$ and $(Ti_2CO_2)_n$ flakes in meV/n as predicted from calculations with the PBE functional. $\Delta E_{\mathrm{AFM-NM}}$ negative values indicate a magnetic ground state; $\Delta E_{\mathrm{AFM-FM}}$ negative values denote that the AFM solution is more stable than the FM one.

Flake	n	$\Delta E_{\mathrm{AFM-NM}}$	$\Delta E_{\mathrm{AFM-FM}}$
Ti_2C	18	-18	1
	36	-30	4
	60	-43	-5
	90	-57	-12
	126	-67	-14
	168	-74	-19
Ti_2CO_2	18	0	0
	60	0	0
	126	0	0

Fig. 1. Top (left panel) and side views (right panel) of (a) bare Ti_2C and (b) Ti_2CO_2 all featuring basal planes with (0001) Miller indexes and the $c(1\times1)$ cell marked with black lines. Panel (c) displays the top (left) and side (right) views of the cuttings to generate (d) $Ti_2C(10\bar{1}0)$, (e) $Ti_2C(11\bar{2}0)$-nonpolar, and (f) $Ti_2C(11\bar{2}0)$-polar surfaces, which include arrows showing the direction on which the width has been measured. Note that even if the $Ti_2C(11\bar{2}0)$-nonpolar and $Ti_2C(11\bar{2}0)$-polar are parallel, they are not equivalent as, due to the ABC stacking of the atomic layers, the atoms they expose are different. The Ti atoms are represented with blue spheres, while the C and O atoms are represented with brown and red spheres, respectively. For (a) and (c), the $c(1\times1)$ cells and the supercells for the rest of Figs. are marked with black lines.

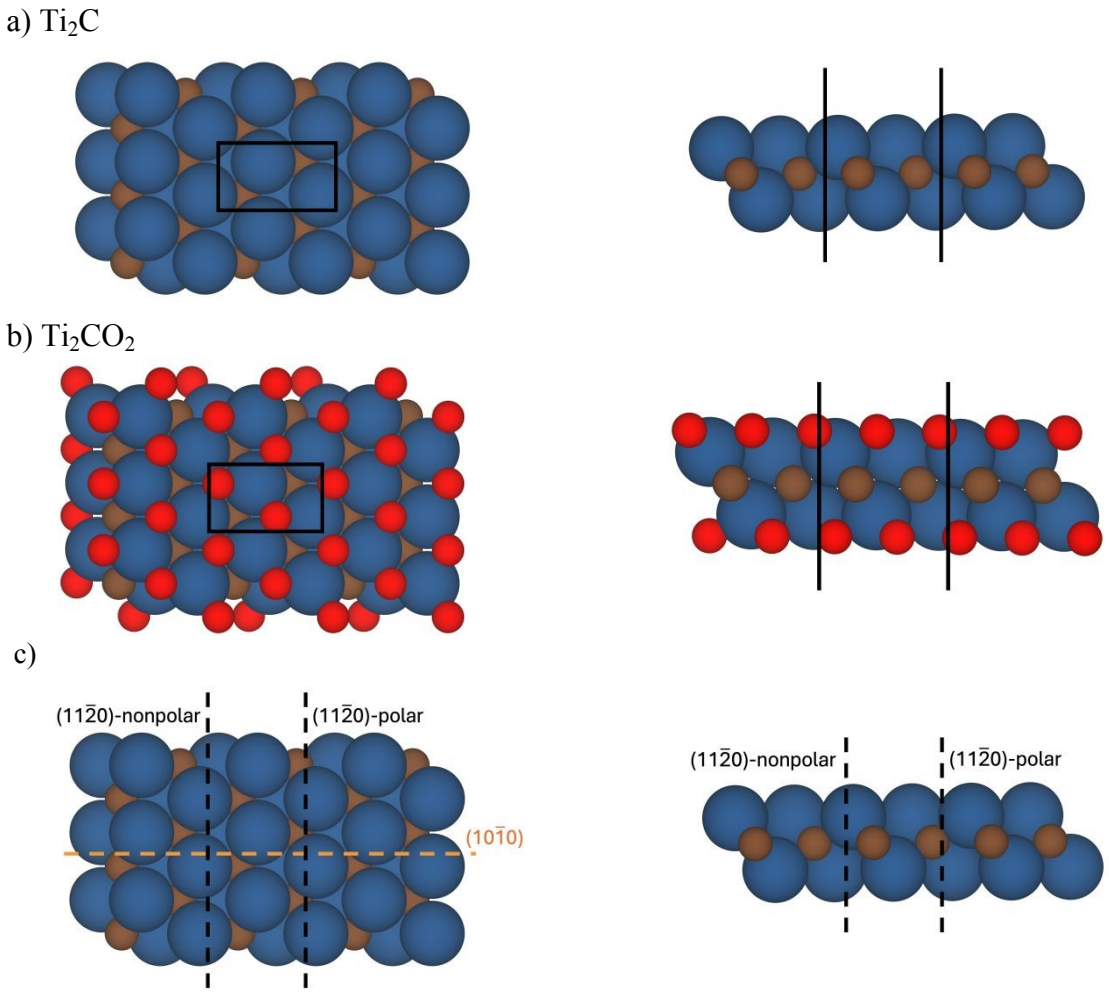

View Article Online
DOI: 10.1039/D5NR02231B

d) $(10\bar{1}0)$ Ti_2C

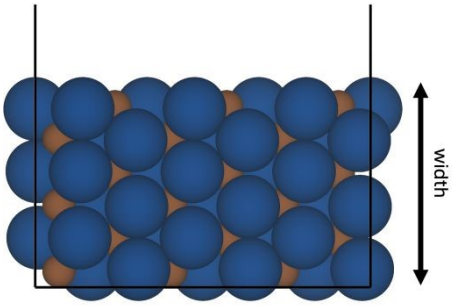

e) $(11\bar{2}0)$-nonpolar Ti_2C

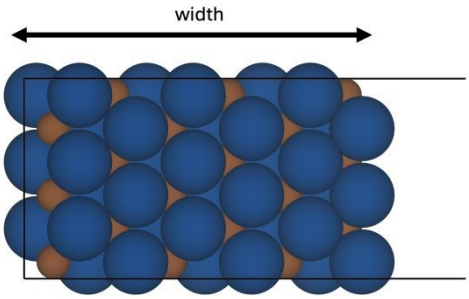

f) $(11\bar{2}0)$-polar Ti_2C

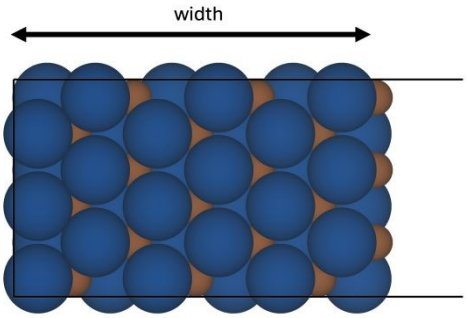

View Article Online
DOI: 10.1039/D5NR02231B

Fig. 2. Top view of $(Ti_2C)_{60}$ flake made from cuts made along the $(10\bar{1}0)$ and $(11\bar{2}0)$-nonpolar planes represented by orange and black dashed lines, respectively, according to the Wulff construction. Colour-coding as in Fig. 1.

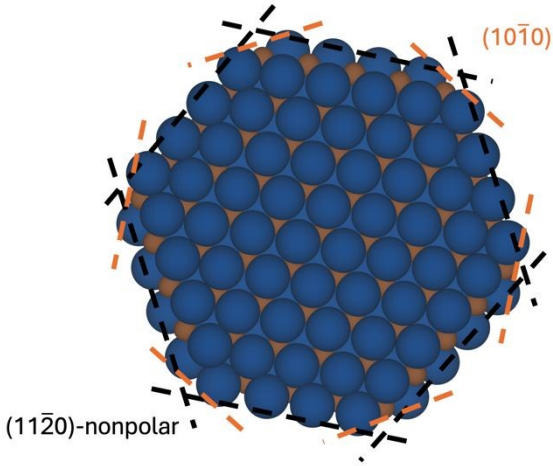

View Article Online
DOI: 10.1039/D5NR02231B

Fig. 3. Top and side view of each optimized and stoichiometric $(Ti_2C)_n$ n=18–168, including their planar diameter, ∅, in nm, and of the O-covered $(Ti_2CO_2)_{18}$, $(Ti_2CO_2)_{60}$, and $(Ti_2CO_2)_{126}$ flakes. Colour-coding as in Fig. 1.

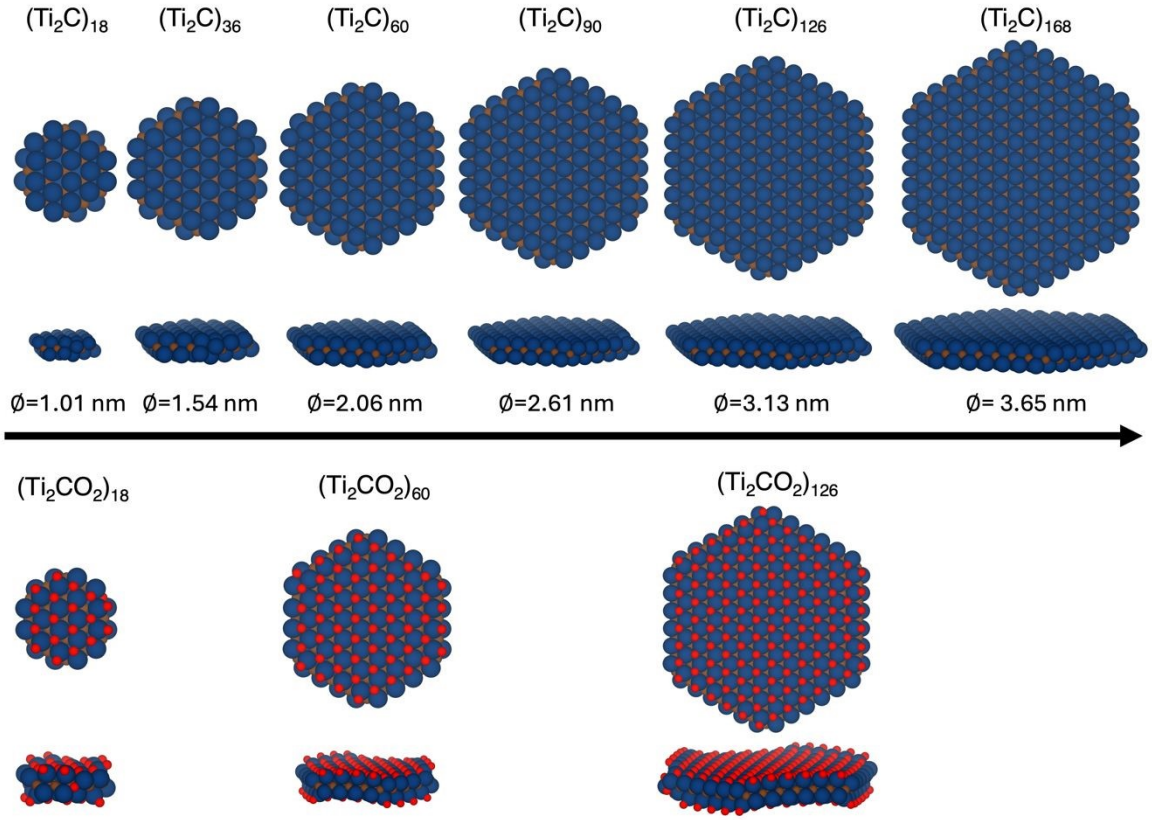

View Article Online
DOI: 10.1039/D5NR02231B

Fig. 4. Average Ti coordination (top panel) and C coordination (bottom panel) for each studied Ti_2C flake as a function of Ti_2C units, *n*. The dashed black lines correspond to the periodic model values.

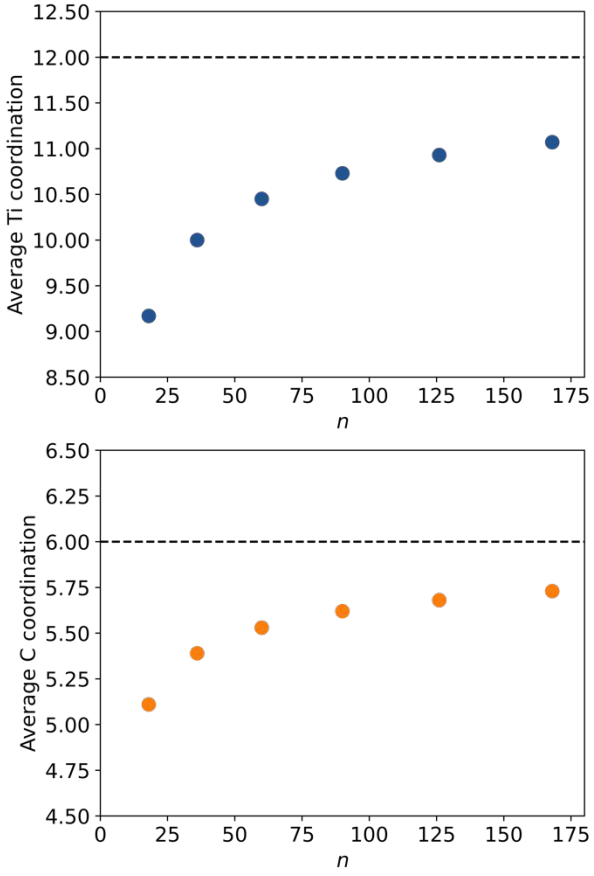

View Article Online
DOI: 10.1039/D5NR02231B

Fig. 5. Relative stability of the most stable isomer to the periodic surface per formula unit n, ΔE in eV/n, thus given per chemical unit (left panel) and formation energy, E_f in eV/n, (right panel) at the NM and AFM solution of each $(Ti_2C)_n$ n=18–168 flake, as a function of Ti_2C units, n. The ΔE and E_f have been calculated following Eq. 2 and 3, respectively. The dashed lines correspond to fitting curves of SCA, whose fitting parameters are gathered in Table S2 from SI.

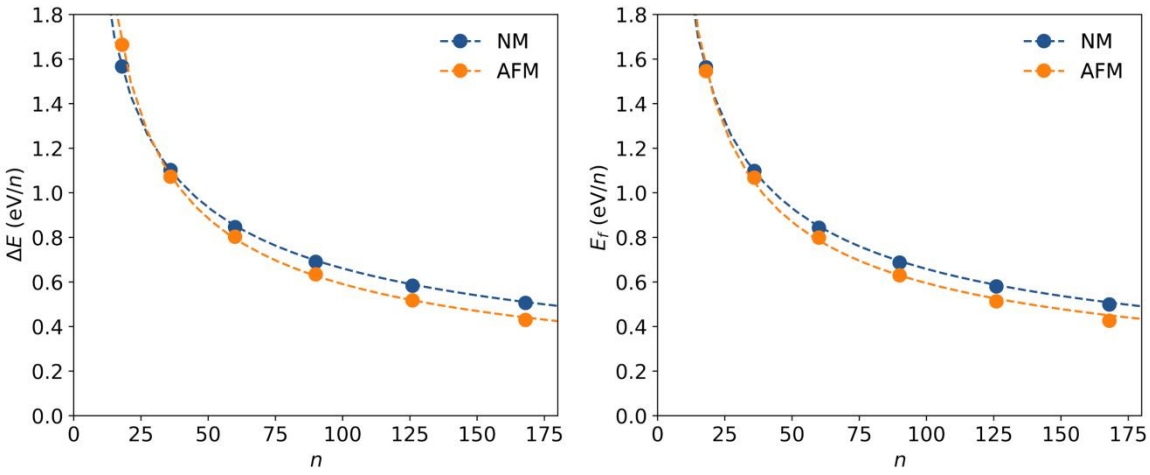

View Article Online
DOI: 10.1039/D5NR02231B

Fig. 6. Band edges for the most stable isomer of each $(Ti_2C)_n$ n=18–168 flake, evolution of Valence Band Maximum (VBM) and Conduction Band Minimum (CBM), for the PBE NM (left panel) and AFM solution (central panel) and at HSE06 NM solution (right panel), as a function of n.

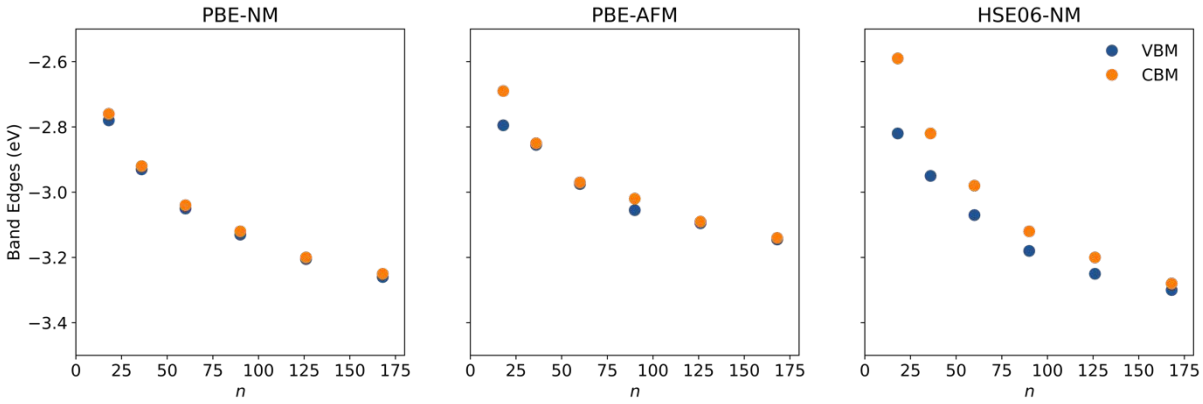

References

(1) M. Naguib, M. Kurtoglu, V. Presser, J. Lu, J. Niu, M. Heon, L. Hultman, Y. Gogotsi and M. W. Barsoum, *Adv. Mater.*, 2011, **23**, 4248–4253.

(2) Y. Gogotsi and B. Anasori, *ACS Nano*, 2019, **13**, 8491–8494.

(3) M. Naguib, V. N. Mochalin, M. W. Barsoum and Y. Gogotsi, *Adv. Mater.*, 2014, **26**, 992–1005.

(4) A. VahidMohammadi, J. Rosen and Y. Gogotsi, *Science*, 2021, **372**, 1165.

(5) J. C. Lei, X. Zhang and Z. Zhou, *Front. Phys.*, 2015, **10**, 276–286.

(6) M. Khazaei, A. Mishra, N. S. Venkataramanan, A. K. Singh and S. Yunoki, *Curr. Opin. Solid State Mater. Sci.*, 2019, **23**, 164–178.

(7) G. Deysher, C. E. Shuck, K. Hantanasirisakul, N. C. Frey, A. C. Foucher, K. Maleski, A. Sarycheva, V. B. Shenoy, E. A. Stach, B. Anasori and Y. Gogotsi, *ACS Nano*, 2020, **14**, 204–217.

(8) I. Persson, J. Halim, H. Lind, T. W. Hansen, J. B. Wagner, L.-Å. Näslund, V. Darakchieva, J. Palisaitis, J. Rosen and P. O. Å. Persson, *Adv. Mater.*, 2019, **31**, 1805472.

(9) V. Kamysbayev, M. Filatov, X. Hu, X. Rui, F. Lagunas, D. Wang, S. K. Fullon, A. Sarycheva, A. Srivastava, M. J. May, L. Balents, Y. Gogotsi and D. V. Talapin, *Science*, 2020, **369**, 979–983.

(10) B. Anasori and Y. Gogotsi, *2D Metal Carbides and Nitrides (MXenes)*, ed. B. Anasori and Y. Gogotsi, Springer, 2019.

(11) M. Khazaei, M. Arai, T. Sasaki, C.-Y. Chung, N. S. Venkataramanan, M. Estili, Y. Sakka and Y. Kawazoe, *Adv. Funct. Mater.*, 2013, **23**, 2185–2192.

(12) N. García-Romeral, Á. Morales-García, F. Viñes, I. de P. R. Moreira and F. Illas, *Phys. Chem. Chem. Phys.*, 2023, **25**, 31153–31164.

(13) D. Ontiveros, F. Viñes and C. Sousa, *J. Mater. Chem. A*, 2023, **11**, 13754–13764.

(14) D. Ontiveros, S. Vela, F. Viñes and C. Sousa, *Energy Environ. Mater.*, 2024, **7**, e12774.

(15) F. Shahzad, M. Alhabeb, C. B. Hatter, B. Anasori, S. M. Hong, C. M. Koo and Y. Gogotsi, *Science*, 2016, **353**, 1137–1140.

(16) T. Yun, H. Kim, A. Iqbal, Y. S. Cho, G. S. Lee, M.-K. Kim, S. J. Kim, D. Kim, Y. Gogotsi, S. O. Kim and C. M. Koo, *Adv. Mater.*, 2020, **32**, e1906769.

(17) A. Iqbal, F. Shahzad, K. Hantanasirisakul, M.-K. Kim, J. Kwon, J. Hong, H. Kim, D. Kim, Y. Gogotsi and C. M. Koo, *Science*, 2020, **369**, 446–450.

View Article Online
DOI: 10.1039/D5NR02231B

(18) G. Boidi, J. C. F. de Queiróz, F. J. Profito and A. Rosenkranz, *ACS Appl. Nano Mater*., 2023, **6**, 729–737.

(19) A. Rosenkranz, M. C. Righi, A. V. Sumant, B. Anasori and V. N. Mochalin, *Adv. Mater*., 2023, **35**, 2207757.

(20) F. Bu, M. M. Zagho, Y. Ibrahim, B. Ma, A. Elzatahry and D. Zhao, *Nano Today*, 2020, **30**, 100803.

(21) Q. Tang, Z. Zhou and P. Shen, *J. Am. Chem. Soc*., 2012, **134**, 16909–16916.

(22) Y. Yang, J. Chen, J. Tang, F. Xing and M. Yao, *J. Phys. Chem. C*, 2021, **125**, 21453–21459.

(23) D. Dolz, R. De Armas, P. Lozano-Reis, Á. Morales-García, F. Viñes, R. Sayós and F. Illas, *ChemCatChem*, 2024, **16**, e202400122.

(24) R. Ramírez Grau, P. Garcia-Aznar, G. Sastre, S. Goberna-Ferrón, O. Pavel, A. Tirsoaga, B. Cojocaru, D. G. Popescu, V. I. Parvulescu, A. Primo and H. García, *J. Am. Chem. Soc*., 2025, **147**, 3315–3332.

(25) H. Zhou, Z. Chen, E. Kountoupi, A. Tsoukalou, P. M. Abdala, P. Florian, A. Fedorov and C. R. Müller, *Nat. Commun*., 2021, **12**, 5510.

(26) L. Meng, L.-K. Yan, F. Viñes and F. Illas, *J. Mater. Chem. A*, 2024, **12**, 7856–7874.

(27) J. D. Gouveia, G. Novell-Leruth, P. M. L. S. Reis, F. Viñes, F. Illas and J. R. B. Gomes, *ACS Appl. Bio Mater*., 2020, **3**, 5913–5921.

(28) K. Xie, J. Wang, S. Xu, W. Hao, L. Zhao, L. Huang and Z. Wei, *Mater. Des*., 2023, **228**, 111867.

(29) J. D. Gouveia, G. Novell-Leruth, F. Viñes, F. Illas and J. R. B. Gomes, *Appl. Surf. Sci*., 2021, **544**, 148946.

(30) S. Zhao, W. Kang and J. Xue, *J. Mater. Chem. C*, 2015, **3**, 879.

(31) L. Hong, R. F. Klie and S. Öğüt, *Phys. Rev. B*, 2016, **93**, 115412.

(32) Y. Zhou, K. Luo, X. Zha, Z. Liu, X. Bai, Q. Huang, Z. Guo, C.-T. Lin and S. Du, *J. Phys. Chem. C*, 2016, **120**, 17143–17152.

(33) B. Vénosová and F. Karlický, *Nanoscale Adv*., 2023, **5**, 7067–7076.

(34) X. Yang, N. Gao, S. Zhou and J. Zhao, *Phys. Chem. Chem. Phys*., 2018, **20**, 19390.

(35) G. Wulff, *Z. Kristallogr*., 1901, **34**, 449–530.

(36) A. S. Barnard and P. Zapol, *Phys. Rev. B*, 2004, **70**, 235403.

View Article Online
DOI: 10.1039/D5NR02231B

(37) C. Loschen, A. Migani, S. T. Bromley, F. Illas and K. M. Neyman, *Phys. Chem. Chem. Phys.*, 2008, **10**, 5730.

(38) A. Migani, K. M. Neyman, F. Illas and S. T. Bromley, *J. Chem. Phys*., 2009, **131**, 064701.

(39) F. Viñes, O. Lamiel-Garcia, F. Illas and S. T. Bromley, *Nanoscale*, 2017, **9**, 10067–10074.

(40) O. Lamiel-Garcia, K. C. Ko, J. Y. Lee, S. T. Bromley and F. Illas, *J. Chem. Theory Comput*., 2017, **13**, 1785–1793.

(41) M. Recio-Poo, Á. Morales-García, F. Illas and S. T. Bromley, *Nanoscale*, 2024, **16**, 8975–8985.

(42) L. Vega, J. Ruvireta, F. Viñes and F. Illas, *J. Chem. Theory Comput*., 2018, **14**, 395–403.

(43) J. Ruvireta, L. Vega and F. Viñes, *Surf. Sci*., 2017, **664**, 45–49.

(44) D. Vázquez-Parga, A. Fernández-Martínez and F. Viñes, *J. Chem. Theory Comput*., 2023, **19**, 8285–8292.

(45) D. González, B. Camino, J. Heras-Domingo, A. Rimola, L. Rodríguez-Santiago, X. Solans-Monfort and M. Sodupe*, J. Phys. Chem. C*, 2020, **124**, 1227–1237.

(46) J. M. Rahm and P. Erhart, *J. Open Source Softw*., 2020, **5**, 1944.

(47) M. Keyhanian, D. Farmanzadeh, Á. Morales-García and F. Illas, *J. Mater. Chem. A*, 2022, **10**, 8846–8855.

(48) I. Persson, J. Halim, T. W. Hansen, J. B. Wagner, V. Darakchieva, J. Palisaitis, J. Rosen and P. O. Å. Persson, *Adv. Funct. Mater*., 2020, **30**, 1909005.

(49) V. Blum, R. Gehrke, F. Hanke, P. Havu, V. Havu, X. Ren, K. Reuter and M. Scheffler, *Comput. Phys. Commun*., 2009, **180**, 2175–2196.

(50) J. P. Perdew, K. Burke and M. Ernzerhof, *Phys. Rev. Lett*., 1996, **77**, 3865.

(51) C. Chang, M. Pelissier and P. Durand, *Phys. Scr*., 1986, **34**, 394–404.

(52) E. van Lenthe, E. J. Baerends and J. G. Snijders, *J. Chem. Phys*., 1994, **101**, 9783–9792.

(53) V. Havu, V. Blum, P. Havu and M. Scheffler, *J. Comput. Phys*., 2009, **228**, 8367–8379.

(54) F. Viñes and F. Illas, *J. Comput. Chem.*, 2017, **38**, 523–529.

(55) F. Knuth, C. Carbogno, V. Atalla, V. Blum and M. Scheffler, *Phys. Commun*., 2015, **190**, 33–50.

(56) H. J. Monkhorst and J. D. Pack, *Phys. Rev. B*, 1976, **13**, 5188.

(57) N. García-Romeral, Á. Morales-García, F. Viñes, I. de P. R. Moreira and F. Illas, *J. Phys. Chem. C*, 2023, **127**, 3706–3714.

(58) Y. Xie and P. R. C. Kent, *Phys. Rev. B*, 2013, 87, 235441.

View Article Online
DOI: 10.1039/D5NR02231B

(59) A. H. Larsen, J. J. Mortensen, J. Blomqvist, I. E. Castelli, R. Christensen, M. Dułak, J. Friis, M. N. Groves, B. Hammer, C. Hargus, E. D. Hermes, P. C. Jennings, P. B. Jensen, J. R. Kermode, J. R. Kitchin, E. L. Kolsbjerg, J. Kubal, K. Kaasbjerg, S. Lysgaard, J. B. Maronsson, T. Maxson, T. Olsen, L. Pastewka, A. Peterson, C. Rostgaard, J. Schiøtz, O. Schütt, M. Strange, K. S. Thygesen, T. Vegge, L. Vilhelmsen, M. Walter, Z. Zeng and K. W. Jacobsen, J. *Phys.: Condens. Matter*, 2017, **29**, 273002.

(60) I. de P. R. Moreira, F. Illas and R. L. Martin, *Phys. Rev. B*, 2002, **65**, 155102.

(61) Á. Morales-García, R. Valero and F. Illas, *J. Phys. Chem. C*, 2017, **121**, 18862–18866.

(62) J. Heyd, G. E. Scuseria and M. Ernzerhof, *J. Chem. Phys.*, 2003, **118**, 8207–8215.

(63) X. Ren, P. Rinke, V. Blum, J. Wieferink, A. Tkatchenko, A. Sanfilippo, K. Reuter and M. Scheffler, *New J. Phys*., 2012, **14**, 053020.

(64) N. García-Romeral, Á. Morales-García, F. Viñes, I. de P. R. Moreira and F. Illas, *Phys. Chem. Chem. Phys*., 2023, **25**, 17116–17127.

(65) P. Lv, Y. L. Li and J. F. Wang, *Phys. Chem. Chem. Phys*., 2020, **22**, 11266–11272.

(66) Q. Wan, S. Li and J. B. Liu, *ACS Appl. Mater. Interfaces*, 2018, **10**, 6369–6377.

(67) M. Sternik and U. D. Wdowik, *Phys. Chem. Chem. Phys*., 2018, **20**, 7754–7763.

(68) V. Natu, J. L. Hart, M. Sokol, H. Chiang, M. L. Taheri and M. W. Barsoum, *Angew. Chem. Int. Ed.*, 2019, **58**, 12655–12660.

(69) R. Johnson, *Masters Series in Physics and Astronomy in Atomic and Molecular Clusters*, 1st ed, Taylor and Francis, 2002.

(70) Á. Morales-García, A. Macià Escatlar, F. Illas and S. T. Bromley, *Nanoscale*, 2019, **11**, 9032.

(71) A. S. Barnard and P. Zapol, *Phys. Rev. B*, 2004, **70**, 235403.

(72) A. S. Barnard and L. A. Curtiss, *Nano Lett*., 2005, **5**, 1261–1266.

(73) O. Lamiel-Garcia, A. Cuko, M. Calatayud, F. Illas and S. T. Bromley, *Nanoscale*, 2017, **9**, 1049.

Data availability statements

View Article Online
DOI: 10.1039/D5NR02231B

The data supporting this article have been included as part of the ESI. Specific data files (files or atomic models) related to this study are available upor request from the corresponding author.